Velocimetry Measurements of Unstart in an Inlet-Isolator Model in Mach 5 Flow

J. L. Wagner*
University of Texas at Austin, Austin, Texas 78712
K. B. Yuceil[†]
Istanbul Technical University, 34469 Istanbul, Turkey
and
N. T. Clemens[‡]
University of Texas at Austin, Austin, Texas 78712

The dynamics of unstart in a floor-mounted inlet-isolator model in a Mach 5 flow are investigated experimentally using particle image velocimetry and fast-response wall pressure measurements. The inlet compression is obtained with a 6-deg ramp and the isolator is a rectangular straight duct that is 25.4 mm high by 50.8 mm wide by 242.3 mm long. Unstart is initiated from the scramjet mode (fully supersonic in the isolator) by deflecting a motorized flap at the downstream end of the isolator. With the flap fully down, the particle image velocimetry data of the started flow capture the characteristics of the isolator boundary layers and the initial inlet reflected shock system. During unstart, the unstart shock system propagates upstream through the inlet-isolator. The particle image velocimetry data reveal a complex, three-dimensional flow structure that is strongly dependent on viscous mechanisms. Particularly, the unstart shock system propagates upstream and induces significant boundary-layer separation. Side-view particle image velocimetry data show that the locations of strongest separation during unstart correlate with the impingement locations of the initial inlet shock as it reflects down the isolator. For example, in the middle of unstart, the unstart shock system is associated with massive separation of the ceiling boundary layer that begins where the first inlet shock reflection impinges on the ceiling. The observation that separation increases at the inlet shock reflection impingement locations is likely due to the fact that the boundary layers in these locations are subject to larger adverse pressure gradients, thus making them more susceptible to separation. During the unstart process, large regions of separated flow form near the floor and ceiling with reverse flow velocities up to about $0.4U_\infty$. These regions of separated, subsonic flow appear to extend to the isolator exit, creating a path by which the isolator exit boundary condition can be communicated upstream. Plan-view particle image velocimetry data show the unstart process begins with separation of the isolator sidewall boundary layers. Overall, the unstart flow structure is highly three-dimensional.

Nomenclature

a	=	speed of sound
C_p	=	specific heat at constant pressure
d_p	=	agglomerated TiO_2 particle diameter
f	=	frequency
f^*	=	normalized frequency $= fL/a_0$
H_0	=	inlet entrance height
h	=	isolator height
Kn	=	Knudsen number
k_B	=	Boltzmann's constant
L	=	model length
M	=	Mach number
P	=	pressure
Re	=	Reynolds number
T	=	temperature
t	=	time
U	=	mean streamwise velocity
u	=	instantaneous streamwise velocity
u_p	=	particle velocity
V	=	mean wall-normal velocity
v	=	instantaneous wall-normal velocity
W	=	mean spanwise velocity
x	=	streamwise coordinate
y	=	wall-normal coordinate
z	=	spanwise coordinate
δ	=	boundary layer thickness
δ^*	=	displacement thickness
ε_{Cal}	=	velocity measurement uncertainty from the image registration process
ε_{Prec}	=	precision uncertainty in mean velocity measurements
ε_{Proc}	=	velocity measurement uncertainty from the data reduction process
$\varepsilon_{\Delta t}$	=	velocity measurement uncertainty due to variations in laser pulse separation times
θ	=	momentum thickness
Λ	=	mean free path
μ	=	dynamic viscosity
ρ_p	=	particle density
σ	=	standard deviation
τ_p	=	particle response time

Subscripts

0	=	stagnation
∞	=	freestream condition
m	=	mean

*Graduate Research Assistant, Center for Aeromechanics Research, Department of Aerospace Engineering and Engineering Mechanics; currently Postdoctoral Appointee, Sandia National Labs, Albuquerque, NM. Member AIAA.
[†]Assistant Professor, Department of Astronautical Engineering, Faculty of Aeronautics and Astronautics. Member AIAA.
[‡]Professor, Center for Aeromechanics Research, Department of Aerospace Engineering and Engineering Mechanics. Associate Fellow AIAA.

I. Introduction

SCRAMJET and ramjet engines are technologies that will enable a future generation of hypersonic missiles, aircraft and space vehicles. A particularly attractive configuration is the dual-mode engine concept proposed by Curran and Stull [1], which allows the engine to act in ramjet mode at lower supersonic to hypersonic flight Mach numbers and then transition to scramjet mode at higher hypersonic flight Mach numbers. Since the introduction of the dual-mode concept in 1963, researchers have aimed to understand the complex flowfields involved and improve engine performance [2–17].

In the dual-mode engine, the inlet and the isolator components serve to provide the compression required for combustion [2]. The isolator is a duct that follows the inlet, connecting it to the combustor. The primary purpose of the isolator, as the name implies, is to isolate the combustion pressure rise from reaching the inlet [2–4]. The ability of an inlet-isolator to provide an increase in static pressure prior to combustion is a pertinent performance measure, as it is an indicator of how much combustion (and therefore how much thrust) can be supported [4]. A variety of parameters affect the maximum static pressure gain, such as the inlet-isolator geometry [4,7–11,13], and the isolator entrance flow profile [5,6]. When the dual-mode engine is in the ramjet mode of operation (flight Mach number of about 3 to 6), a strong precombustion shock system is required to slow the flow at the combustor entrance to subsonic velocities [2,3]. Typically, the precombustion shock system takes the form of a "shock-train" in the isolator [3]. If the isolator is long enough, a mixing region will follow the shock-train resulting in additional compression. The shock-train and mixing region combination is referred to as a pseudoshock in the literature [7]. In a pseudoshock the maximum pressure increase can approach, but is always less than, the value obtained from a single normal shock at the isolator entrance Mach number [7]. For higher flight Mach numbers greater than about six, it is desirable to have combustion at supersonic velocities to avoid dissociation [3]. Up to about $M_\infty = 8$ [14], the levels of supersonic combustion required to generate thrust can produce pressures great enough to cause boundary layer separation. In this case, through separation, a shock-train with a supersonic core flow then forms in the isolator [3]. Therefore, in the flight Mach number regime of about 6 to 8, an isolator is required to sustain supersonic combustion [3]. For flight Mach numbers greater than about eight [14], the levels of combustion required to create thrust no longer result in significant boundary layer separation. In this case the engine is said herein to act as a "pure" scramjet and the isolator is no longer required to sustain the combustion pressure increase. As a general rule of thumb, the Mach number at the combustor inlet (or, equivalently the Mach number at the isolator exit) is equal to 0.38 times the flight Mach number [3]. Note this relation was derived under the assumption of adiabatic compression for flight in the lower stratosphere ($T_\infty = 220$ K) and in the hypersonic limit [3].

Another function of the isolator is to reduce the sensitivity of the inlet to combustor pressure perturbations [2–4]. Disturbances due to combustion can lead to a transient process known as unstart [2,3]. Specifically, if the combustion pressure rises to a value that cannot be matched by the precombustion shock system, the engine will unstart [2,3]. During unstart, the original inlet-isolator shock system is "disgorged" and it can eventually take the form of a detached bow shock that resides upstream of the inlet entrance [3]. The unstart process can be severe with high transient pressure loads [3,18] and it can lead to a loss of engine thrust [3].

Several experimental studies have focused on unstart [18–22]. In a Mach 5.3 flow, Weiting [18] induced unstart in a three-dimensional scramjet model by inserting a cylindrical pin to create blockage. The peak pressures during unstart were up to 20 times greater than the started flow pressures. High-frequency-response pressure measurements were used to calculate the propagation velocities of the unstart shock system throughout the model. In the lab frame of reference, these velocities ranged from 10 to 27 m/s (≈ 1 to 4% of U_∞). The work of Rodi et al. [19] investigated unstart in a two-dimensional dual-mode model in a Mach 4 flow. The model was pressurized (and

eventually unstarted) by raising a flap that was downstream of the isolator in the model's nozzle section. Unstart propagation velocities were reported to range from 55 to 70 m/s (≈ 8 to 10% of U_∞). In addition, in some configurations following unstart, oscillatory (periodic) unstarted flows with frequencies of about 300 Hz were reported. It was noted that the oscillation frequency was about 1.2 times the resonant frequency predicted for an ideal half-wave resonator (i.e., the frequency if their dual-mode model acted as a resonator with two free boundaries). Hawkins and Marquart [20] unstarted a two-dimensional supersonic/hypersonic inlet with flaps at the rear of the model in flows with Mach numbers ranging from 2.5 to 5. The inlet flow was observed to be highly separated after unstart. Other experiments have studied unstart events induced by combustion. For example, in a Mach 4 flow, Shimura et al. [21] unstarted their three-dimensional combusting scramjet model by increasing the mass flow rate of hydrogen fuel. It was observed that fuel flow rates near that which caused unstart resulted in distinct pressure spikes upstream of the isolator entrance. A more fundamental experimental investigation by O'Byrne et al. [22] studied unstart events in a model scramjet combustor with entrance Mach numbers of both 2.5 and 3.8. For both Mach numbers supersonic combustion was seen to lead to the formation of a normal shock that propagated upstream. The flow behind this normal shock was seen to have a Mach number near unity. It was therefore suggested that heat addition led to thermal choking, which forced the shock upstream during unstart.

CFD simulations have also been aimed at understanding unstart [23–26]. Sato and Kaji [23] stated that as unstart occurs, the "boundary layer flow spreads and pushes out the main flow" of the engine inlet. Neaves et al. [24] simulated unstart of the dual-mode engine model studied by Emami et al. [4] and McDaniel and Edwards [26] simulated unstart in the model scramjet used by Masuya et al. [16]. In both CFD simulations, unstart events were seen to be associated with shock-induced separation. In addition, McDaniel and Edwards [26] noted that unstart appeared to occur as a result of shock-induced separation and not thermal choking. Furthermore, at the end of the unstart process, the isolator flow was seen to be highly three-dimensional; specifically, the flow in the spanwise center plane flow was supersonic, whereas flow near the sidewalls was reversed.

Although unstart has been the subject of several studies, much remains unknown about unstart dynamics and the flow structure that develops during the process. This paper describes an experimental study of unstart in an inlet-isolator model that was mounted on the floor of a Mach 5 wind tunnel. The inlet-isolator, which consists of a simple compression surface inlet and a straight rectangular isolator, is meant to represent a simplified form of a dual-mode scramjet inlet-isolator. To initiate unstart, a flap was deflected at the exit of the isolator. In a previous study [27], unstart in the same inlet-isolator model was investigated by using high-speed schlieren imaging, and fast-response wall pressure measurements. The data were used to characterize the flow structure during unstart and to determine the relevant time-scales involved in unstart and unstarted flows. Unstart was seen to progress upstream in the form of a shock system defined to be the "unstart shock system." This unstart shock system took the form of oblique separation shocks and not the form of a normal shock as was reported by O'Byrne et al. [22]. The pressure near the isolator exit increased by nearly 500% during unstart. The unstart shock system progressed upstream through the isolator at an average velocity of 3.5% of the freestream velocity. Similar to that of previous computational work [24,26], it was observed that the upstream progression of unstart was associated with shock-induced separation. The previous work also characterized unstarted flows in the inlet-isolator. A "high-amplitude oscillatory unstarted flow" with a frequency of 124 Hz ($0.11 a_0/L$) was always seen to follow unstart. The current paper seeks to increase further the understanding of unstart flow physics by using particle image velocimetry (PIV) measurements to provide quantitative flow structure information. PIV measurements were made in the streamwise-transverse (side-view) as well as the streamwise-spanwise plane (plan-view). In addition to the PIV data, wall pressure and schlieren data are presented to provide a more complete picture of the unstart process.

II. Experimental Setup

A. Facility and Test Model

The experimental data were acquired in the Mach 5 blowdown wind tunnel at the University of Texas at Austin. Tanks with a volume of 4 m^3 (141 ft^3) at a pressure of 17.6 MPa (2550 psi) supplied the wind tunnel air. A pressure transducer (Setra model 204) and a J-type thermocouple monitored the stagnation conditions. A static pressure port at the test section entrance that was connected to a factory calibrated precision dial gage (Heise Model CMM) was used to measure the freestream pressure. Tests were conducted at freestream pressures of $P_\infty = 5.38 \pm 0.28$ kPa (0.78 ± 0.04 psia), stagnation temperatures of $T_0 = 335 \pm 4$ K (603 ± 7 R) and stagnation pressure of $P_0 = 2517 \pm 35$ kPa (365 ± 5 psia). Assuming isentropic flow from the plenum to test section, the pressure ratio P_∞/P_0 gives a freestream Mach number of 4.9. The freestream velocity was determined with PIV to be 740 m/s (2430 ft/s) [27], which using Sutherland's formula for viscosity gives a freestream unit Reynolds number of 66.5×10^6 m^{-1} (20.3×10^6 ft^{-1}). The test section had a constant area with a width of 152.4 mm (6 in.), a height of 177.8 mm (7 in.) tall and a length of 762 mm (30 in.). For optical access, fused-silica windows, 381 mm (15 in.) long and 50.8 mm (2 in.) tall were placed in the test section side walls.

The inlet-isolator model was mounted on the floor of the test section and is shown in Fig. 1. Figure 1a shows a top-view of the model with the ceiling removed and Fig. 1b shows a side-view of the model with the portside sidewall removed. The nondimensional coordinate system is in units normalized by the isolator height h. The model's internal inlet consisted of a 6-deg compression ramp. The inlet sidewall sweep angle was 53.5 deg with respect to the y axis. The height, H_0, at the inlet entrance was 34.9 mm (1.375 in.) and the height at the entrance of the isolator section (i.e., the throat) was 25.4 mm (1 in.). The inlet was 90.7 mm (3.57 in.) long and the constant area isolator was 242.3 mm (9.54 in.) long. The aspect ratio (width: height) at the inlet entrance was 1.45 and the isolator aspect ratio was 2. A mechanical flap driven by a rack and pinion drive system was raised to simulate the combustor pressure rise. In the fully-down position the leading edge of the flap was at the streamwise coordinate of $x/h = 12.9$. The model was seen to unstart at a flap angle of 26 ± 0.6 deg [28]. At this angle the leading edge of the flap translates to $x/h = 12.7$. Further details on the model and flap drive system design are given in [27,28].

Since the model was floor-mounted, the inlet ingested the test section floor boundary layer, which was turbulent and quite thick in comparison to the inlet height. Upstream of the inlet, the floor boundary layer developed naturally under nearly adiabatic conditions [29,30]. The velocity profile of the incoming boundary layer was determined with PIV measurements. The boundary layer temperature profile was then inferred from the velocity profile by using the Crocco–Busemann relation $C_p T_0 = C_p T + \frac{u^2}{2}$ [31]. The Crocco–Busemann relation is derived under the assumptions of steady adiabatic flow, $Pr = 1$, and where the boundary layer approximations are valid. The density profile was determined assuming a
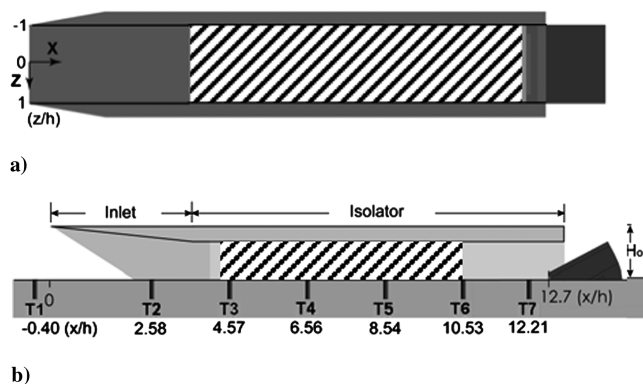
constant boundary layer pressure and under the assumption of a perfect gas. The floor boundary layer was then determined to have the following properties: 99% thickness $\delta = 19.3$ mm (0.76 in.), displacement thickness $\delta^* = 8.7$ mm (0.34 in.), momentum thickness $\theta = 0.77$ mm (0.030 in.), and Reynolds number based on momentum thickness, $Re_\theta = 50,000$. These values are in good agreement with those obtained with Pitot probe measurements at similar test conditions [32]. The other inlet wall (ceiling and sidewalls) boundary layers developed naturally.

B. Fast-Response Pressure Measurements

Wall pressure measurements were made with seven fast-response transducers (effective frequency responses of about 50 kHz) that were flush mounted on the floor near the spanwise centerline of the model. The streamwise transducer positions are denoted T1–T7 on the schematic of Fig. 1b. T7 was at the spanwise center of the model whereas T1–T6 were shifted slightly off center, 4.1 mm in the starboard direction to accommodate a laser-exit window for the PIV. T2–T7 (Kulite XCQ-062-50A) had ranges of 0–350 kPa (0–50 psia) and T1 (Kulite XCQ-062-15A) had a range of 0–100 kPa (0–15 psia). Each of the transducer signals were amplified with a wideband differential DC amplifier (Dynamics model 7525). The signals were then low-pass filtered using an active filter (DL model 4302 or Ithaco S30) and digitally sampled at a rate of 192 kHz or 25 kHz with 2 A/D cards (National Instruments DAQ PCI-6110E) housed in a personal computer. The filter cutoff frequency was 50 kHz for the data sampled at 192 kHz and 12.5 kHz for the data sampled at 25 kHz. An in house developed Labview code controlled the 2 A/D cards. Least squares linear regression fits based on pressures measured with a factory calibrated precision dial gage (Heise model CMM) were used to calibrate the transducers. Each of the pressures used to generate the calibration lines fell within 1% of the corresponding linear fit values. The uncertainty due to run-to-run variations, calibration-to-calibration variations and electronic noise is estimated to be ± 1.6 kPa (± 0.23 psi). Thus, assuming the uncertainty sources to be independent, the total uncertainty in each pressure value is estimated to be the root-sum-square value of ± 1.6 kPa and 1% of the given pressure (i.e., the calibration nonlinearity).

C. PIV System and Particle Tracking Considerations

Figure 2 shows a schematic of the PIV system setup for plan-view measurements. The seeding system can be seen in the left of the figure. The PIV seed-particles were titanium dioxide (Evonik P25) with a manufacturer specified primary diameter of 0.02 μm. Owing to agglomeration, the actual seed-particle size is significantly larger, and this issue is discussed further below. Compressed nitrogen drove the seeding system. The particles were seeded upstream of the stagnation chamber using a two-stage fluidized-bed seeder followed by a cyclone separator. Further details on the seeder system can be
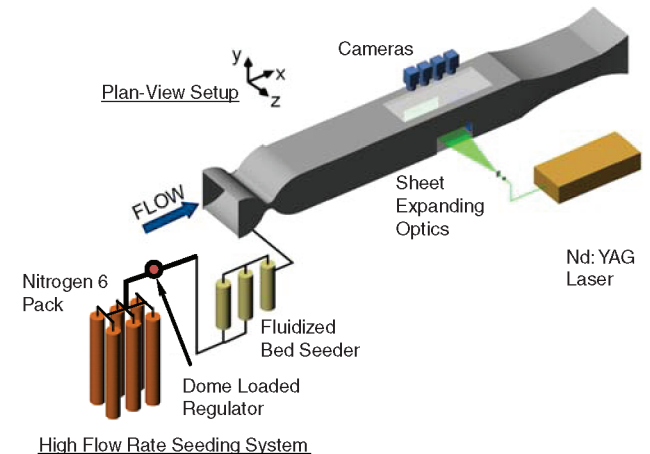

Fig. 1   PIV fields of view: a) hatched rectangle indicating the plan-view PIV field of view and b) side-view PIV field of view.

Fig. 2   Schematic showing the wide-field PIV system setup for plan-view measurements.

found in Hou [33]. The wide-field PIV system utilized pulsed laser sheets from a dual-cavity flashlamp pumped Nd:YAG laser (Spectra Physics PIV 400) separated in time by 2.00 μs. The laser repetition rate was 10 Hz. The fields of view corresponding to the plan- and side-view measurements are given in Figs. 1a and 1b, respectively.

For the plan-view, the laser sheets entered and exited the wind tunnel test section through fused-silica side windows and passed through the acrylic isolator sidewalls. The sheets were at the wall-normal (transverse) center of the model ($y/h = 0.5$). The laser energy of each pulse was about 140 mJ and the thickness of each sheet was approximately 1.4 mm. Digital image pairs were acquired with four Kodak MegaPlus ES 1.0 cameras (1024×1024 pixels) which imaged the flow through a fused-silica test section window and the acrylic isolator ceiling. The cameras were fitted with 105 mm focal length camera lenses (Nikon AF Micro-Nikkor) and arranged side-by-side to capture a field of view that extended in the streamwise direction from $x/h = 4.0$ to 12.5 for a total length of 216 mm. The lens aperture setting was 16 for the plan-view experiments. The entire internal span of the isolator from $z/h = -1.0$ to $+1.0$ (51 mm) was imaged.

For the side-view, the laser sheets entered the wind tunnel test section through a fused-silica top window, passed through an acrylic isolator ceiling and exited through an acrylic isolator/test section floor window. The sheets were offset 3.2 mm to the port side of the spanwise center of the model isolator. The laser energy of each pulse was about 100 mJ and the thickness of each sheet was approximately 1.4 mm. Digital image pairs were acquired with three Kodak MegaPlus ES 1.0 cameras. The cameras were arranged side-by-side to capture a field of view of 150 mm (5.9 h) long by 25.4 mm (1.0 h) high. The lens aperture setting was eight for the side-view experiments. The field of view covered a portion of the visible isolator as shown in Fig. 1b.

PIV images were processed with the LaVision DaVis 7.21 software. Prior to correlation computations, each image was background subtracted using the sliding minimum background subtraction function built into the software. This served to remove some of the background noise due to accumulation of particles on the tunnel and isolator walls. Correlations were then computed using the normalized cross correlation function with a Gaussian weighted interrogation window. The interrogation window size was 32×32 pixels (for each pass), which corresponded to linear resolutions of 1.95×1.95 mm and 1.78×1.78 mm for the plan- and side-views, respectively. An overlap of 50% was used resulting in final fields of 219×51 vectors and 173×28 vectors for the plan- and side-views, respectively. Four passes (three adaptive passes) were used to calculate the final vector field. On each pass, a signal-to-noise filter removed vectors with a ratio of highest correlation peak to second highest correlation peak ratio less than 1.2 (within the range suggested by Keane and Adrian [34]). In addition, the velocity data were filtered with a standard 3×3 median filter. In the median filter, the components of the velocity vector in question were compared with the median velocity components of the neighboring vectors. Vectors having a velocity component with a deviation outside the range of $\pm 2\sigma$ (where σ is the standard deviation) from the median were removed. Missing vectors were interpolated using a 3×3 local average technique. The percentage of valid vectors in the PIV data was seen to vary according to the flowfield being measured. Further details are given in the results sections.

A source of bias error can arise in PIV if the particles do not faithfully track flow velocity changes. A measure of the particles' ability to track velocity changes in the flow is the particle response time, τ_p [35]. By definition, a particle experiencing a step change in velocity will take a time τ_p to reach 63% of the velocity step change. Hou [33] investigated the response time of the same TiO$_2$ particles used in this study. His measurements were based on the relaxation distance of particles as they passed through a shock wave. For example, the response time τ_p of particles traveling through a Mach 2 normal shock was measured to be about 2.6 μs. From this response time the effective agglomerated diameter of the particles was estimated to be about 0.26 μm. However, for the flow conditions

reported herein, the particle response time due to a sudden velocity change is expected to differ from that at Mach 2. This is clear upon inspection of the relation for τ_p given by Erbland [36]:

$$\tau_p = \frac{\rho_p d_p^2}{18\mu}[1 + Kn(2.492 + 0.84\exp(-0.435/Kn)] \qquad (1)$$

where μ is dynamic viscosity of the gas (calculated herein with Sutherland's formula), ρ_p is the particle density, d_p is the particle density and Kn is the Knudsen number, which is equal to the mean free path (Λ) divided by the particle diameter. This work includes PIV measurements of fully supersonic flow (when the flap is fully down), and of the unstart process. To get an estimate of the particles' ability to track velocity fluctuations within these flows, three particle response times were calculated using Eq. (1) and the particle diameter measured by Hou [33] of 0.26 μm. These response times were for freestream flow, an oblique shock generated by a Mach 5 flow over a 6-deg wedge, and a Mach 5 normal shock. For the freestream flow, the particle $Kn = 0.27$ and τ_p computes to be 7.1 μs. Note that in this case, the rarefied-flow term of Eq. (1) substantially increases the calculated particle response time to 1.7 times the value that would correspond to pure Stokes drag. The freestream τ_p was used to estimate particle tracking in the turbulent floor boundary layer of the started flow, which was similar to the floor boundary layer in the test section outside of the isolator. Samimy and Lele [37] suggested that for particles to reliably follow velocity fluctuations in a turbulent mixing layer, the Stokes number, which is defined as $St = \tau_p/\tau_f$, where τ_f is the characteristic flow timescale, must be less than about 0.5. The characteristic timescale in this Stokes number criterion was based on the vorticity thickness as the characteristic length scale. In the current work, in the turbulent boundary layer, the characteristic length scale based on outer-scale or large-scale structures is taken to be the boundary layer thickness, δ. Therefore, the timescale based on large-scale structures is taken to be $\tau_f = \delta/\Delta U$, where ΔU is the characteristic velocity difference. The minimum velocity measurements made in the floor boundary layer were about 400 m/s. Taking the characteristic velocity difference to be the difference between this minimum and the freestream velocity gives $\tau_f = 55$ μs and $St = 0.13$. Therefore, the particles should faithfully track large-scale velocity fluctuations within the turbulent floor boundary layer of the started flow. When the flap was in the fully-down position, the flow consisted of a series of oblique shock and expansion wave reflections. To get an idea of the particles' ability to follow the started flow, the particle response time after a 6-deg oblique shock ($Kn = 0.16$) was calculated using Eq. (1). Based on this particle response time of 4.5 μs, particles will travel a distance of about 3.5 mm to reach 63% of the velocity induced by a 6-deg oblique shock [28]. Recall that the spatial resolution of the PIV data is about 2 mm (without overlap). Therefore, the started flow velocity data in regions corresponding to oblique shocks are expected to appear smoothed with respect to the PIV spatial resolution.

During unstart, a strong shock system was seen to propagate upstream through the inlet-isolator model. To estimate the ability of particles to track the flow through this unstart shock system, the unstart shock system was modeled as a Mach 5 normal shock and the response time of particles with flow conditions behind this shock was calculated. Using the flow conditions behind a Mach 5 normal shock ($Kn = 0.06$) and Eq. (1) gives a response time τ_p of 0.75 μs. This corresponds to a distance of 0.4 mm that the particles will travel to reach 63% of the velocity step change [28]. This suggests that the ability to resolve the unstart shock system will be limited by the spatial resolution of the data and not the particle response time. It is also important to estimate the particles' ability to faithfully track the flow downstream of the unstart shock system. As will be discussed, the flow downstream of the unstart shock system was seen to contain prominent shear layers with velocity differences across the layers being as high 1000 m/s. The particle response time at flow conditions downstream of a Mach 5 normal shock was used to estimate particle tracking capabilities in these shear layers. The requirement of Samimy and Lele [37] that St should be less than 0.5

was used to estimate the characteristic flow widths over which particles may be expected to track velocities. The characteristic flow width corresponding to $St = 0.5$, $\tau_p = 0.75$ μs and $\Delta U = 1000$ m/s is 1.5 mm. This estimate suggests that the particles should be able to faithfully track large-scale velocity fluctuations of large-scale flow structures (i.e., structures thicker than 1.5 mm) within the shear layers that exist during unstart.

D. Uncertainty in the PIV Measurements

This section presents a summary of the velocity uncertainties in the PIV measurements. Uncertainties associated with laser pulse time variations ($\varepsilon_{\Delta t}$), image registration (ε_{Cal}), precision uncertainty (ε_{Prec}), camera noise, and the data reduction process (ε_{Proc}), were considered. A more detailed analysis can be found in [28].

1. Image Registration, Laser Pulse Separation Time (Δt) and Precision Uncertainties

Small variations in laser pulse separation time resulted in an uncertainty ($\varepsilon_{\Delta t}$) of 0.1% a given velocity [38]. Placement of the calibration grid used for image registration also contributed to the uncertainty. For the side-view PIV measurements, the image registration process involved placing the calibration grid at the laser sheet location by measuring its distance from the test section sidewalls with a ruler. This resulted in slight differences in magnification that resulted in a velocity uncertainty (ε_{Cal}) of 0.5% a given velocity value. For the plan-view measurements the grid was placed on a platform that rested on the floor, which resulted in a more repeatable placement as compared with the side-view grid placement. Therefore, for the plan-view measurements the calibration uncertainty was lower at 0.1% a given velocity value. Mean velocity fields are given for the fully supersonic started flow (i.e., flap fully-down). For these data, the precision uncertainty (ε_{Prec}) for the mean velocity was taken to be $2\sigma_U/\sqrt{n}$, where σ_U is the standard deviation of U and n is the number of PIV images used to compute the mean.

2. Data Reduction (Processing) Uncertainties

After the nomenclature of Beresh [39], "advanced algorithms" are defined to be those that utilize interrogation window deformation and fractional window displacements (e.g., [40]). Such algorithms are employed by the LaVision DaVis 7.21 processing software used in the current study. In comparison to "classical algorithms" (e.g., Keane and Adrian [34], and Westerweel [41]), advanced algorithms have been shown to improve vector detection probabilities and reduce velocity measurement errors [40]. However, there does not appear in the literature a reliable method to estimate uncertainties associated with applying such advanced algorithms to actual PIV data [39]. Naturally, the uncertainties will be dependent on the flow and the PIV system. In absence of a prescribed method, the following technique was employed to estimate the uncertainties associated with the data reduction process (i.e, processing uncertainty). For the side-view PIV, the three cameras were aligned in a way such that the upstream field of view sufficiently overlapped the middle field of view to produce two independent measurements of the column of vectors at $x/h = 6.5$. Similarly the middle field of view sufficiently overlapped the downstream field of view to produce two independent measurements of the column of vectors at $x/h = 8.4$. The comparison of vectors given by the two independent measurements allowed for the uncertainties associated with the PIV data reduction process and camera noise to be estimated [28]. The same technique with similar overlap was applied to the plan-view data as well. Since the uncertainties involved in the data reduction process (ε_{Proc}) were dependent on the flowfield of interest they are presented in the results section. For the mean data presented the total uncertainty was taken to be the root-sum-squares value of $\varepsilon_{\Delta t}$, ε_{Cal}, ε_{Prec}, and ε_{Proc}. Similarly, for the instantaneous data, the total uncertainty was taken to be the root-sum-squares value of $\varepsilon_{\Delta t}$, ε_{Cal}, and ε_{Proc}.

III. Results

This paper first presents the flow structure of the fully supersonic flow within the inlet-isolator model, which is obtained with the flap in the fully-down position. The flow structure during the unstart process, as revealed with the PIV measurements, is then discussed.

A. Fully Supersonic Started Flow Side-View PIV

Mean velocity fields of the fully supersonic started isolator were acquired in a field of view covering nearly 2/3 of the isolator as seen in Fig. 1b. Ninety vector fields from one wind tunnel test were used to calculate the mean. The percentage of valid (noninterpolated) vectors is about 93% for the dataset. Only valid vectors were used to calculate the mean. For the mean streamwise velocities, the maximum uncertainties occur near the wall and are about ± 17 m/s. Outside of the floor boundary layer and at about $y/h = 0.8$, the uncertainties decrease to about ± 6 m/s [28].

The mean velocity fields of the fully supersonic started isolator are shown in Fig. 3. For comparison, a schlieren image, taken at the same steady-state condition, but not simultaneously, is shown in Fig. 3a. The three ramp shock reflections are seen in the image (arrows 1–3). The mean V-velocity (wall-normal component) and U-velocity (streamwise component) contour plots are shown in Figs. 3b and 3c, respectively. Figure 4 shows a schematic of the system of shocks and expansions in the inlet-isolator for the fully supersonic flow, which is based on previous schlieren imaging [27]. Comparison of Fig. 3b and 4 shows that the V-contour plot reveals the system of reflected shocks and expansions within the isolator. Flow at the far left of the image is turned downward by the oblique shock generated by the 6-deg compression ramp. Farther downstream, the flow in the upper portion of the isolator is then turned parallel to the ceiling by the inlet shoulder expansion fan. The first reflected oblique shock turns the flow in the lower portion of the isolator parallel to the floor. From about $x/h = 6$ to 9 the flow is predominantly inclined upward due to the system of reflected shock and expansion waves. The flow then turns parallel to the floor and then downward due to continued reflections of this system. The U-velocity contour plot of Fig. 3c shows the thick floor boundary layer in the isolator exhibits a nearly constant thickness until a streamwise location of about $x/h = 6$. From this streamwise location to about $x/h = 8$, a noticeable increase in boundary layer thickness is evident, which is due to the impingement of the inlet expansion wave (e.g., Fig. 4). The boundary layer thickness then remains nearly constant until about $x/h = 10$. Figure 3c also shows the presence of the thin isolator ceiling boundary layer. After $x/h = 7$, the ceiling boundary layer grows at a substantially higher rate. The representative schlieren image of Fig. 3a shows this growth occurs after the impingement point of the first reflected oblique shock (arrow A).

Figure 3d gives the mean Mach number distribution for the fully supersonic flow. Mach numbers were calculated by first inferring the mean temperature from the mean velocity by using the Crocco–Busemann relation [31]. The Mach number is then obtained from U, V, and the local speed of sound computed from the local temperature. W was not measured in this plane, although its contribution to the mean velocity magnitude and therefore Mach number is expected to be negligible. Figure 3d shows the flow expands to near the freestream Mach number in the upper half of the isolator between $x/h = 5$ and 6. This is expected since in this region, the flow has passed through the compression ramp oblique shock and then through the inlet shoulder expansion fan. The theoretical Mach number for this sequence from shock-expansion theory is 4.87. The Mach number in the lower portion of the isolator entrance is seen to decrease to less than two near the floor. Farther downstream, the Mach number decreases along the duct centerline to about 3.5 as the floor boundary layer thickness increases downstream of $x/h = 6$. A similar decrease in Mach number is seen near the ceiling after the increased ceiling boundary layer growth downstream of $x/h = 7$. Finally, the Mach number in between these regions of increased boundary layer growth decreases to about 4 from about $y/h = 0.6$ to 0.8. Note that an isolator exit Mach number (or, equivalently a combustor inlet Mach number) of 4 corresponds to a flight Mach
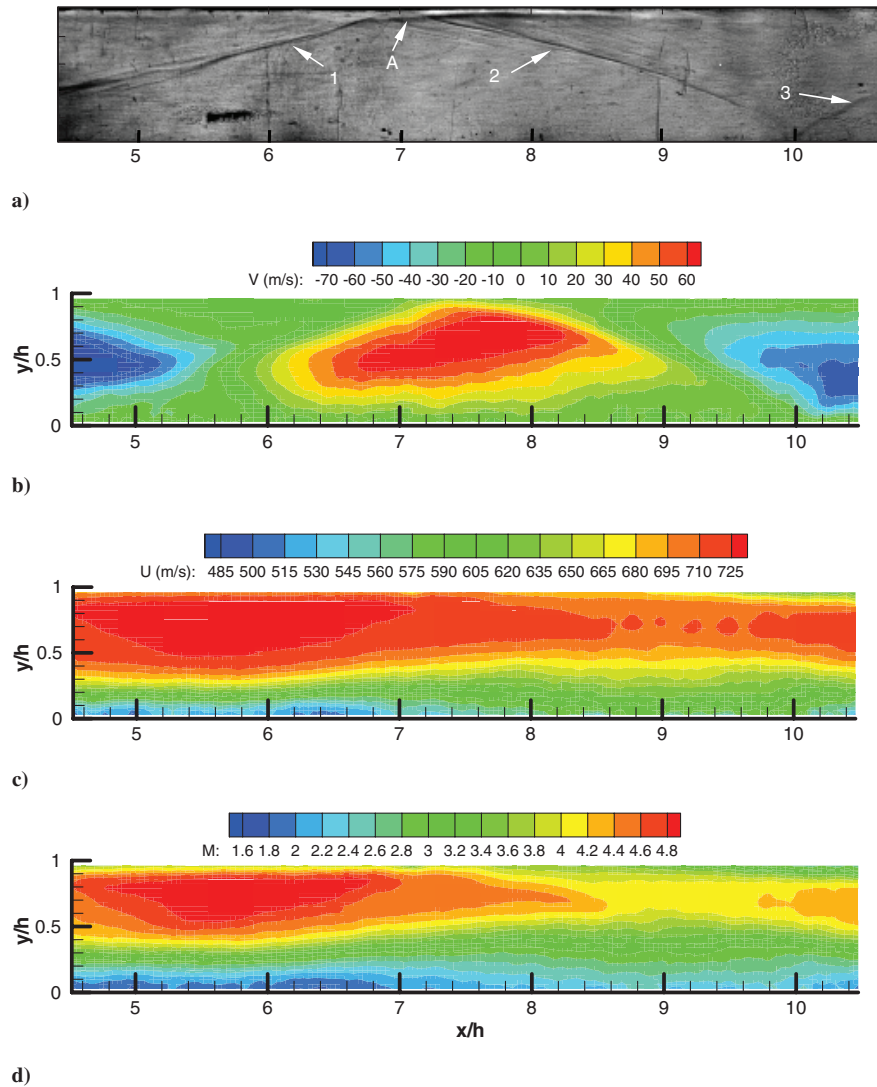
a)

b)

c)

d)

Fig. 3   Flowfield structure for the fully supersonic long isolator: a) representative schlieren image in the PIV field of view (arrows 1–3 point to the three compression ramp shock reflections and arrow A points to the ceiling impingement point of the first reflection), b) mean (based on the 90 vector fields) wall-normal velocity contours, c) mean streamwise velocity contours, and d) Mach number contours.

number of about 10.5 [3]. Therefore, the fully supersonic started flow can be thought of as being analogous to that occurring in a pure scramjet [14].

B. Unstart Process Side-View PIV

1.   Overview

In an actual scramjet, fluctuations in the heat release rate could result in increased thermal-blockage effects or boundary layer separation, and therefore lead to unstart. This section describes the unstart process from the pure scramjet mode discussed above.

In a previous study, the initiation of unstart was seen to be associated with intense boundary layer separation near the isolator exit [27]. At the beginning of the unstart process, the flap shock and the third reflection of the compression ramp shock impinged and
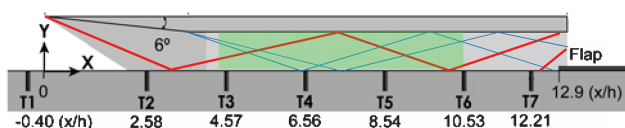

Fig. 4   Schematic of the system of shocks and expansions obtained from schlieren images for fully supersonic (started) flow. Shock waves are shown with red lines, expansion waves with blue lines. PIV field of view is shown by green shade.

interacted on the ceiling. As a result, the ceiling boundary layer separated forming a separation shock. The flap shock and separation shock formed the "head" of the "unstart shock system." The "unstart shock system" is defined to be that which propagates upstream through the model during the unstart process. The "head" is the upstream limit of this unstart shock system. The unstart shock system should not be confused with the initial shock system consisting of the first oblique shock followed by the three reflected oblique shocks. A "pseudosequence" of the unstart process is presented in Fig. 5. With the 10 Hz PIV system of this study, one image pair could be captured every 100 ms. However, the unstart process occurred in a period of about 10 ms; therefore, it was not possible to capture more than one set of PIV data per unstart event. Furthermore, the onset of unstart ($t = 0$) was not repeatable enough to guarantee that a given unstart event could be captured at the time of the PIV acquisition. Thus, in order to increase the likelihood for acquiring PIV data during unstart, the model was unstarted and restarted up to 30 times during a given wind tunnel run, although typically only about one of these 30 cases successfully captured some part of the unstart event. Wind tunnel runs were repeated until a sufficient number of PIV images were captured to enable a pseudosequence of the unstart process to be generated. Of course, this technique relies on the flow structure during unstart being highly repeatable, and the schlieren imaging indicates that this is indeed the case [28]. The procedure used to obtain the pseudosequence is as follows. For each unstart event, pressure data are acquired, and the onset of unstart ($t = 0$) is
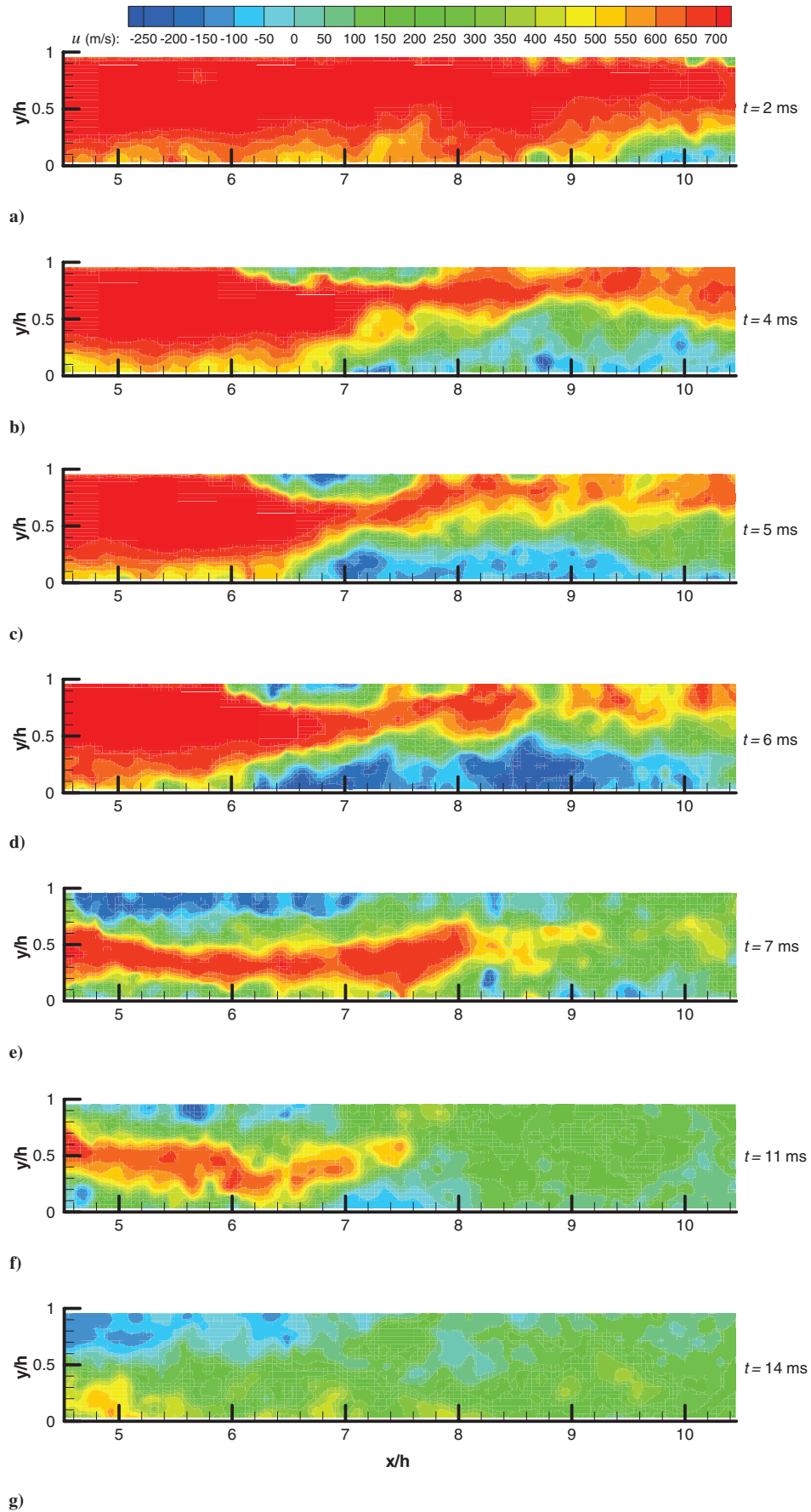
Fig. 5   Streamwise velocity contours for the unstart pseudosequence obtained via side-view PIV: a) 2 ms, b) 4 ms, c) 5 ms, d) 6 ms, e) 7 ms, f) 11 ms, and g) 14 ms into the unstart process.

estimated from the T7 pressure time history [27]. Once the time of unstart onset is known then the time when the PIV data were taken, with respect to unstart onset, can be determined. Repeatability studies show that the time delays from unstart onset (such as those shown in Fig. 5) have a standard deviation of about 1.3 ms.

The percentage of valid vectors for the unstart pseudosequence dataset is 82%. Uncertainties were the highest in separated flow regions that developed during unstart. With upstream propagation, the unstart shock system created large velocity gradients as well as seeding nonuniformities, which were responsible for correlation degradations as compared with the fully supersonic started flow. Thus the dominant source of uncertainty during the unstart process was $\varepsilon_{\text{Proc}}$. The u and v uncertainties are estimated to be ± 102 m/s ($\pm 0.138 U_{\infty}$) and ± 45 m/s ($\pm 0.061 U_{\infty}$), respectively. Again, more details on the uncertainty analysis are given in [28].

2. Upstream Progression of Unstart

This section uses the sequence of streamwise velocity contours shown in Fig. 5 to show how the isolator flow structure evolves as the unstart shock system moves upstream. In addition, Figs. 6–10 provide further details of this process at the selected times of 2, 5, 7, 11 and 14 ms, respectively. Included in these figures are representative schlieren images, representative wall pressure distributions, and instantaneous velocity vector plots. The representative schlieren images and PIV data were not acquired simultaneously, but rather during different unstart events. The schlieren images were selected by comparing the T7 pressure values recorded at the time of the schlieren image acquisition to the T7 pressure values recorded at the time of the PIV data acquisition. However, due to T7 pressure fluctuations, there were seen to be several times for which the T7 pressures were equal. Therefore, the representative schlieren image was then selected based on the further requirement that it have the most similar flow structure to that which could be inferred from the PIV data. The pressure distributions given in Figs. 6–10 correspond to those taken at the time of the schlieren image not the PIV data.

Figure 6 at $t = 2$ ms, shows the flow structure where the unstart shock system has propagated to near the downstream edge of the field of view. Previous work [27] showed the unstart shock system tends to propagate to this position first with a separation of the isolator ceiling boundary layer that occurred near the ceiling impingement point of the third ramp shock reflection. Further upstream propagation then

tends to occur with an increase in separation of the floor boundary layer near the floor impingement location of the second ramp shock reflection [27]. This separation of the floor boundary layer is seen in the schlieren image of Fig. 6a (arrow A). The velocity vector plot of Fig. 6b suggests that unstart has progressed to about $x/h = 9$ along the isolator floor.

Figure 5b at $t = 4$ ms, shows that unstart has progressed upstream to the floor location of about $x/h = 6.5$. In addition, low velocity fluid indicates the unstart shock system intersects the isolator ceiling at the approximate location of $x/h = 6$.

Figure 5c at $t = 5$ ms, shows the strength of reverse flow near the ceiling and floor has increased compared with $t = 4$ ms. Figure 7 provides additional flow structure information at this time during unstart. The representative schlieren image of Fig. 7a shows that the ceiling boundary layer has separated (arrow A) with the upstream propagation of the unstart shock system. This ceiling separation was seen to occur near the impingement location of the first reflection of the compression ramp shock (e.g., arrow A in Fig. 3). Figure 7a also shows that the wall pressure at T4 to T6 has increased in response to the crossing of the unstart shock system. The velocity vector plot of Fig. 7b shows that the unstart shock system has taken the form of two separation shocks with one shock intersecting the floor near $x/h = 6.5$ and the other intersecting the ceiling near $x/h = 6$. Both the vector and streamwise velocity plot of Fig. 5c show that unstart has induced regions of reversed flow near the ceiling and floor. The velocity magnitude of this reversed flow is between 100 and 200 m/s. The PIV data show that the current PIV system is successfully able to resolve the unstart flow structure. In addition, the PIV data provide flow structure information in low speed regions where the density gradients are not high enough to show structure in the schlieren image of Fig. 7a. The Mach number contour plot at $t = 5$ ms is shown in Fig. 7c. At the far left of the figure, the Mach number is close to the freestream value of 4.9 at the top of the isolator and it decreases to about 2 in the thick floor boundary layer. Regions of predominantly subsonic flow are seen downstream of the floor and ceiling separation shocks. The floor subsonic region extends from about the floor separation shock location to the right edge of the image. It is likely that this subsonic region continues until the isolator exit. If this is the case, then the exit area decrease imposed by the flap is "communicated" through this subsonic region.

In the streamwise velocity contour plot of Fig. 5d, taken at $t = 6$ ms, the extent of floor and ceiling separation has increased with
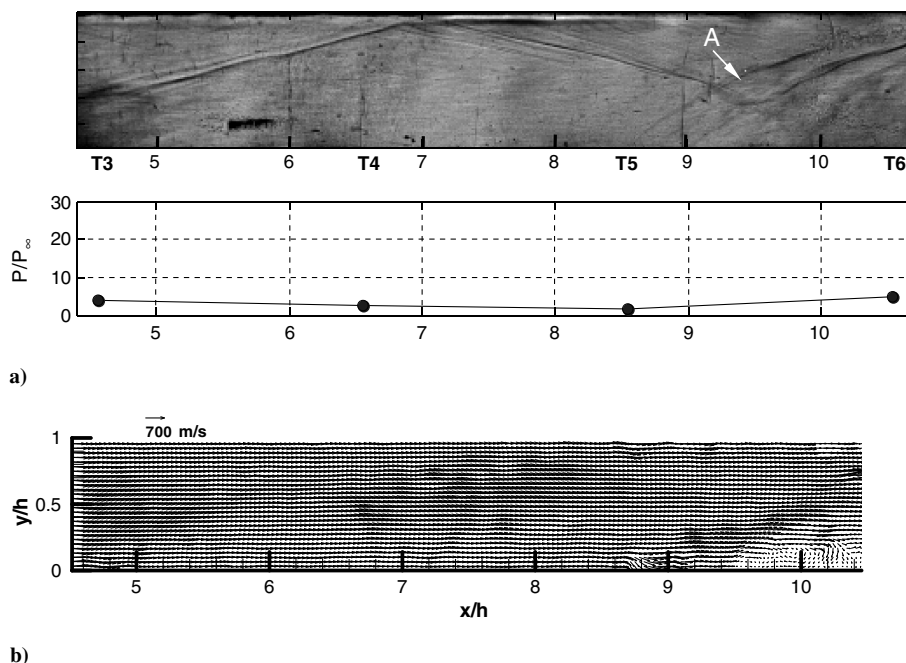

Fig. 6   Instantaneous flow structure during unstart at $t = 2$ ms: a) representative schlieren image and corresponding pressure distribution (arrow A points to the separation location of the floor boundary layer) and b) velocity vectors.
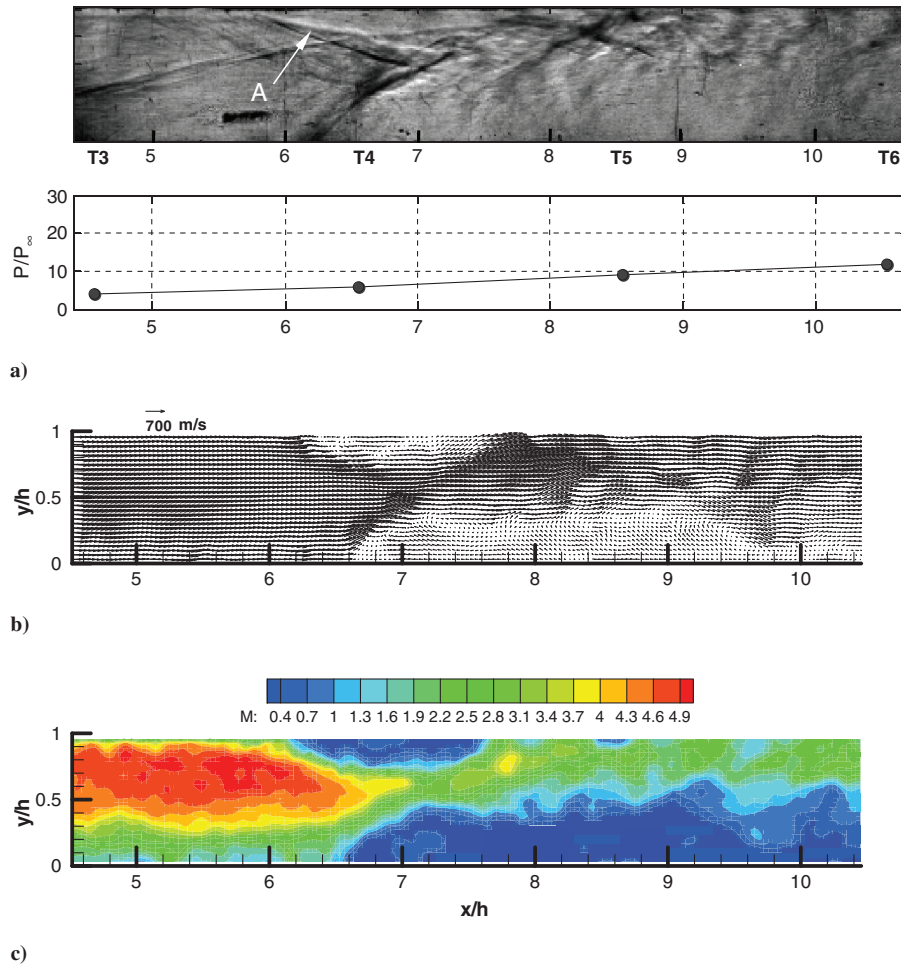
a)

b)

c)

Fig. 7 Instantaneous flow structure during unstart at $t = 5$ ms: a) representative schlieren image and corresponding pressure distribution (arrow A points to the separation location of the ceiling boundary layer), b) velocity vectors, and c) M contours.

respect to Fig. 5c. In addition, the magnitude of reverse flow has increased compared with Fig. 5c and the maximum reverse velocities have reached nearly 300 m/s. The shear layers seen in Fig. 5d create very high velocity gradients. For example, at $x/h = 6.6$ and from the floor to $y/h = 0.5$, the streamwise velocity goes from near -300 m/s to 700 m/s in only about 12 mm.

In the u-velocity contour plot of Fig. 5e, taken 7 ms into unstart, the flow structure is substantially altered. The corresponding detailed flow information given in Fig. 8 shows that the unstart shock system has progressed through the upstream portion of the isolator with increased separation of the ceiling boundary layer. The ceiling separation point has progressed out of the field of view of the representative schlieren image of Fig. 8a (arrow A). Figure 8a also shows that the isolator pressure distribution has increased further compared with that in Fig. 7a. In addition, the increased pressure at T3 indicates that the unstart shock system has crossed this transducer location ($x/h = 4.57$). The velocity vector plot of Fig. 8b and u-velocity contour plot of Fig. 5e show a region of reverse flow on the ceiling from $x/h = 0$ to 7. The maximum measured reverse streamwise velocity is about -250 m/s in this region. Owing to the strong separation shock associated with the ceiling separation, the v-velocity (plot not shown) is about -150 m/s at the isolator entrance near the wall-normal center portion of the isolator. The ceiling separation shock is also seen in the representative schlieren image (arrow B). Although altered, the schlieren image shows the first reflected shock remains in the field of view (arrow C). Downstream of this shock and near the floor around $x/h = 6$, the velocity vector plot shows the flow direction returns to being parallel to the wall. Farther downstream, the flow becomes more uniform probably owing to the high levels of mixing created by the strong shear layers. For example, Fig. 5e shows that downstream of

$x/h = 9$, the streamwise velocity is fairly uniform at about 300 m/s over most of the isolator height.

Figure 5f shows the streamwise velocity plot at $t = 11$ ms where the unstart shock system has progressed further upstream. In addition, Fig. 9 provides more flow structure details at this unstart time. Also, Fig. 11a shows the T1 and T7 pressure time histories for the unstart event corresponding to the data of Figs. 5f and 9. At the time of the PIV image pair acquisition, the unstart shock system has crossed T1 ($x/h = -0.4$), which is upstream of the inlet entrance ($x/h = 0$). This is evident by the distinct pressure increase at about $t = 9.8$ ms. Previous work [27] has shown the unstart shock system to leave the inlet in the form of a strong oblique shock. This oblique shock is referred to herein as the "unstart oblique shock." At the time of the PIV data acquisition, Fig. 11a shows the T7 pressure to be in the middle of a peak pressure "plateau." The schlieren image of Fig. 9a shows what appears to be separated flow entering the isolator entrance (arrow A). Previous work [27] has suggested this separated flow originates in the inlet section at the ceiling, due to the impingement of the unstart oblique shock. The separated flow appears to impinge on the isolator floor at a location of about $x/h = 6$ (arrow B). In Fig. 9a, the isolator pressure distribution has increased compared with Fig. 8a. The velocity vector plot of Fig. 9b also shows the separated flow entering the isolator entrance. Consistent with the schlieren image, the velocity vector plot shows the separated flow appears to impinge on the floor at about $x/h = 6$. Downstream of this impingement, Fig. 9b shows what appears to be a separation shock intersecting the floor near $x/h = 6.8$. A flow recirculation region then follows from about $x/h = 7$ to 8. Downstream of $x/h = 8$, Fig. 5f shows that the u-velocity distribution is much more uniform likely owing to high levels of mixing.
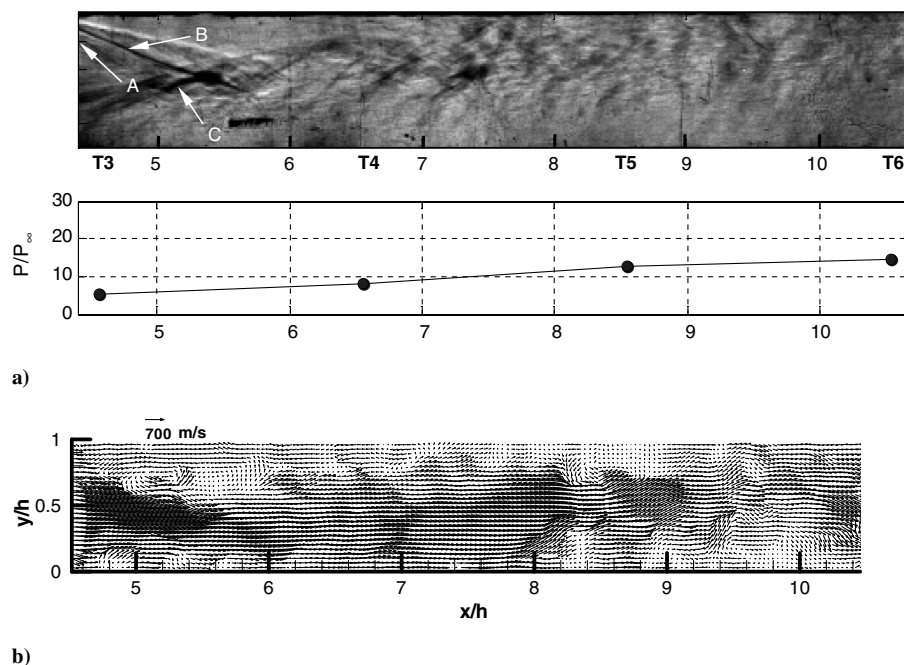
Fig. 8   Instantaneous flow structure during unstart at $t = 7$ ms: a) representative schlieren image (arrow A points to the separation point of the ceiling boundary layer, arrow B points to a ceiling separation shock, and arrow C shows the first reflected shock, which is altered by unstart) and corresponding pressure distribution and b) velocity vectors.

Figure 5g shows the streamwise velocity distribution for the unstart time of $t = 14$ ms and Fig. 10 provides additional flow structure details at this time. Also, Fig. 11b shows the T7 pressure to be at the end of a pressure plateau. Previous work [27] has shown that the other isolator floor pressures (T3–T6) tend to increase with increased T7 plateau duration. Figure 10a shows the isolator pressure distribution has increased further compared with the $t = 11$ ms distribution of Fig. 9a. Overall, the velocity data of Figs. 5g and 10b show a much more uniform flow in the isolator compared with the previous figures of the pseudosequence. Still, Figs. 5g and 10b show a region of reverse flow near the ceiling from $x/h = 4.5$ to 6.5. The

peak streamwise reverse velocity in this region is measured to be about 150 m/s. This separated flow is likely due to the impingement of the unstart oblique shock on the inlet ceiling.

Previous work [27] has shown that with increasing time, the unstart oblique shock tends to propagate far enough upstream to become a bow shock that passes over the inlet ceiling. As the bow shock propagates upstream, the isolator pressures decrease to a minimum. Following this pressure minimum a periodic unstarted flow with high pressure fluctuations occurs [27].

The PIV results confirm that the propagation of the unstart shock system in the isolator is associated with flow separation. At $t = 2$ ms
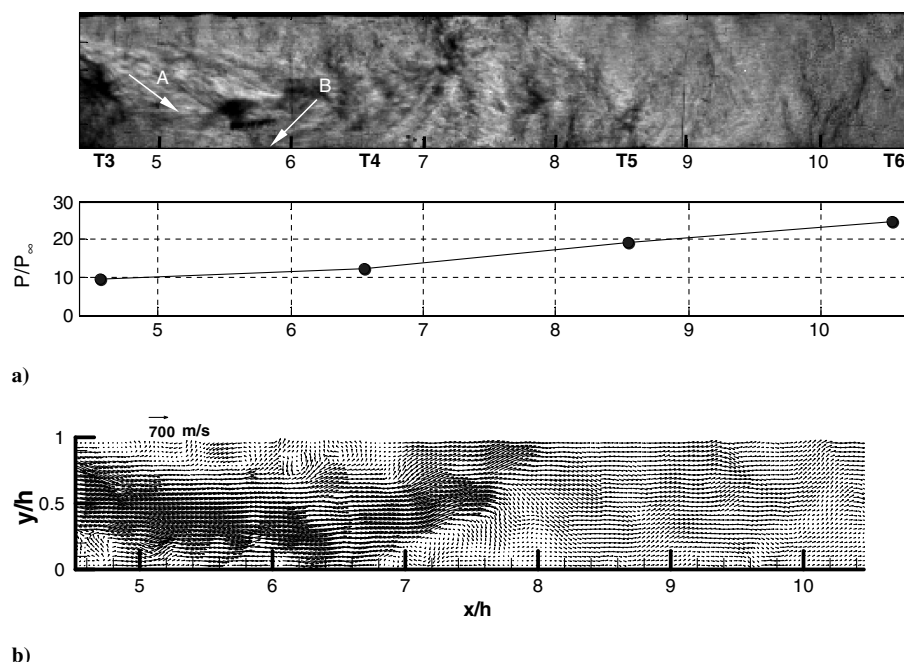

Fig. 9   Instantaneous flow structure during unstart at $t = 11$ ms: a) representative schlieren image (arrow A points in the direction of the separated flow entering the isolator, and arrow B points to the approximate floor impingent location of the separated flow) and corresponding pressure distribution and b) velocity vectors.
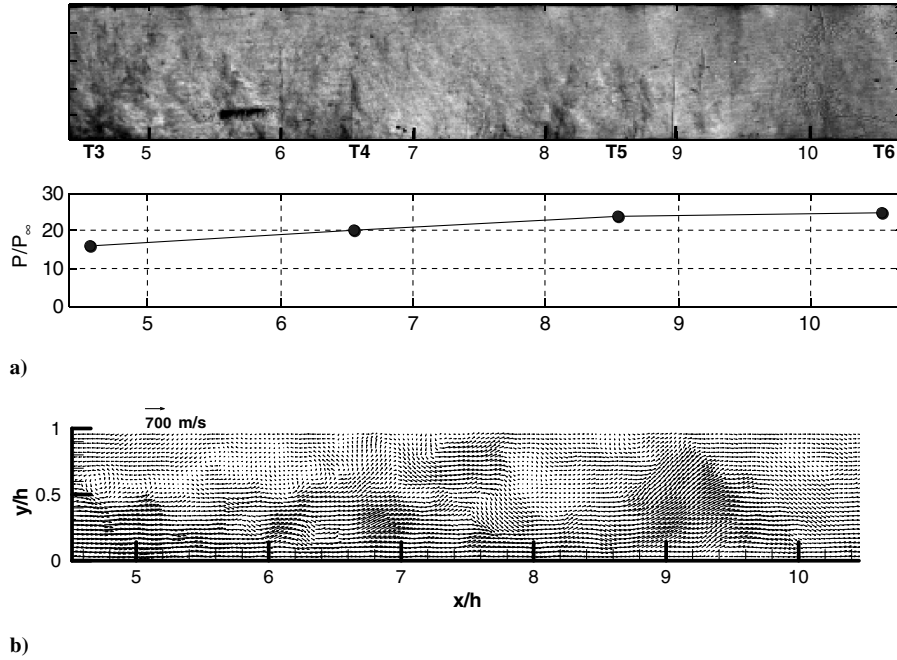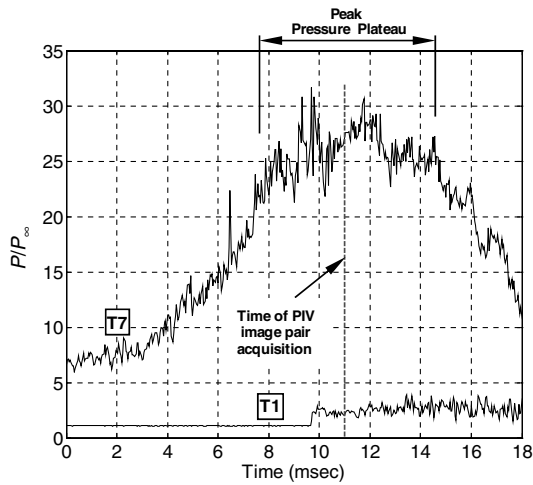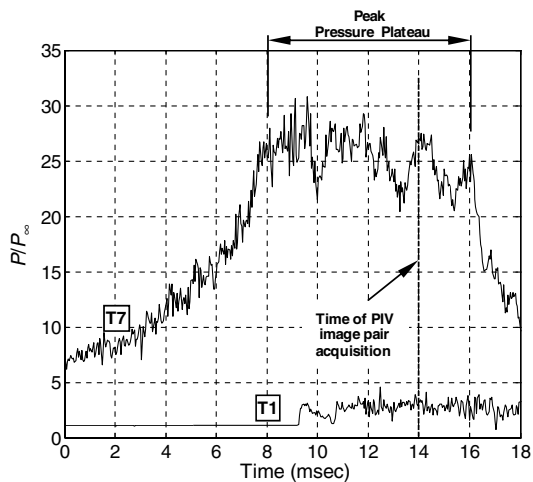
Fig. 10 Instantaneous flow structure during unstart at $t = 14$ ms: a) representative schlieren image and corresponding v pressure distribution and b) velocity vectors.

a)

b)

Fig. 11 Pressure histories showing the time of PIV image pair acquisition for the unstart process pseudosequence at pressure plateau: a) $t = 11$ ms and b) $t = 14$ ms.

(Figs. 5a and 6), the upstream propagation of the unstart shock system is first noticed with separated flow near the floor impingement point of the second reflected shock of the initial oblique shock system. At $t = 5$ ms (Figs. 5c and 7), the unstart shock system is seen to induce significant separation of the ceiling boundary layer. This ceiling boundary layer separation seems to begin near the ceiling impingement point of the first reflected shock of the initial oblique shock system. The PIV pseudosequence indicates that as unstart progresses upstream, strong shock-induced separation occurs first near the floor and then near the ceiling. This shift from the floor to ceiling of the shock-induced separation appears to be related to the location of the impingement points of the initial reflected shocks. Since the flow separates in regions of preexisting adverse pressure gradients, it appears that unstart progresses upstream taking the "path of least resistance." Therefore, these results suggest the unstart flow structure is dependent on inlet geometry.

C. Unstart Process Plan-View PIV

1. Overview

Figure 12 shows a pseudosequence of u-velocity contour plots during the unstart process. Figures 12a–12f correspond to times of $t = 0, 2, 3, 6, 8$ and 10 ms, respectively. Recall that repeatability studies show that the time delays from unstart onset (such as those shown in Fig. 12) have a standard deviation of about 1.3 ms. The field of view plane is at the wall-normal center height of $y/h = 0.5$ and it covers nearly the entire isolator (Fig. 1a). The percentage of valid vectors for the plan-view unstart pseudosequence dataset is 87%. The u-velocity uncertainty [28] is estimated to be ± 63 m/s ($\pm 0.085 U_\infty$). Note this uncertainty is lower than that corresponding to the side-view unstart sequence. This is primarily because the seeding densities were higher in the plan-view plane since it was at the wall-normal centerline and it did not contain the lower portion of the thick floor boundary layer.

2. Upstream Progression of Unstart

Figure 12a shows the wall-normal center plane flow for the flap in the fully-down position or for the fully supersonic flow. Most of the entire flowfield in Fig. 12a consists of high-speed fluid with velocities near 700 m/s. A few regions of lower speed fluid are observed because the measurements were taken within the turbulent floor boundary layer ($y \approx 0.66\delta$). In Fig. 12b at $t = 2$ ms, the unstart
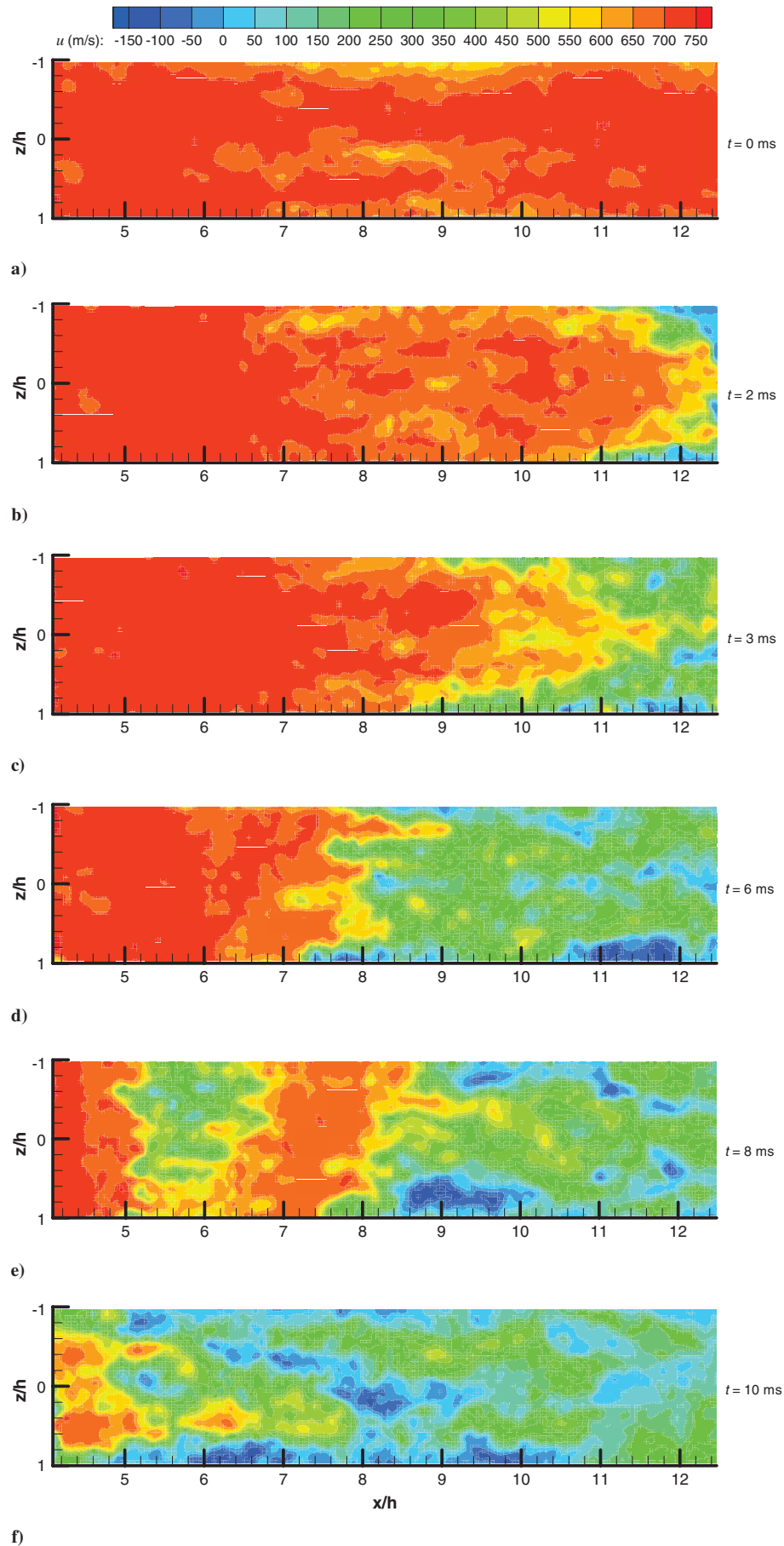
Fig. 12   Streamwise velocity contours for the unstart pseudosequence obtained via plan-view PIV: a) 0 ms, b) 2 ms, c) 3 ms, d) 6 ms, e) 8 ms, and f) 10 ms into the unstart process.

shock system is seen at the far right of the figure with separation of the sidewall boundary layers. In Fig. 12c at $t = 3$ ms, unstart has progressed further upstream along the isolator sidewalls to about $x/h = 8.5$. In comparison, the spanwise centerline flow is seen to be high-speed until the streamwise location of about $x/h = 10$. These data indicate that at the wall-normal center plane, the unstart shock system tends to move upstream first with sidewall boundary layer separation. In Fig. 12d at $t = 6$ ms, the unstart shock system is at the streamwise location of about $x/h = 7.5$. While unstart is three-dimensional, there is not the clear pattern like in Figs. 12b and 12c where unstart progressed first along the isolator sidewalls. Rather, the unstart shock appears undulated along the spanwise direction. Ganapathisubramani et al. [42] observed similar undulations in a ramp-induced shock-wave/boundary layer interaction in a Mach 2 flow. The undulated shock shape was seen to conform to long, streamwise regions of high and low velocity fluid present in the floor boundary layer. Noting the approximate location of $x/h = 7.5$ of the undulated shock in Fig. 12d and looking to Fig. 5d of the side-view pseudosequence, it is apparent that the undulated shock in Fig. 12d is a floor separation shock. In Fig. 12e at $t = 8$ ms, the isolator entrance flow has a velocity of about 700 m/s up until the streamwise location of $x/h = 5$. The velocity then decreases to about 300 m/s. Farther downstream along the spanwise centerline, the velocity then increases to about 650 m/s at $x/h = 7$ and then decreases back to about 300 m/s at $x/h = 8.4$. Comparing the streamwise velocity of Fig. 12e to that at $y/h = 0.5$ in Fig. 5e, shows similar streamwise velocities at similar streamwise locations. This indicates that the flowfield seen in Fig. 12e is a result of a prominent shear layer similar to that seen in Fig. 5e. Figure 12e shows that downstream of $x/h = 8$, the flow is three-dimensional with low speed and reversed flow occurring around $x/h = 8.5$ along the port sidewall and around $x/h = 9$ along the starboard sidewall. Finally, Fig. 12f shows the isolator flow at a time just after the unstart shock system has crossed T1 upstream of the inlet ($x/h = -0.40$). The isolator entrance still contains regions of fast fluid with velocities of about 700 m/s near the spanwise center, whereas the flow near the sidewalls contains predominantly reverse flow. This flow structure is similar to the three-dimensional flowfield observed during unstart in the computational study of McDaniel and Edwards [26].

IV. Conclusions

The flow structure of the unstart process was investigated experimentally in an inlet-isolator model mounted on the floor of a Mach 5 wind tunnel using PIV and simultaneous fast-response wall pressure measurements. The model consisted of an inlet with a 6-deg compression ramp followed by a rectangular isolator that was 25.4 mm high by 50.8 mm wide by 242.3 mm long. The incoming boundary layer thickness was about 19 mm, which was a large fraction of the inlet height of 34.9 mm. Unstart from the scramjet mode was initiated by raising a flap at the exit plane of the isolator. PIV measurements were made in both a streamwise-transverse plane (side-view) and a streamwise-spanwise plane (plan-view). The side-view plane covered nearly 2/3 of the isolator and the plan-view plane covered almost the entire isolator.

The PIV system was able to successfully resolve the flowfields of interest in the isolator. Side-view PIV measurements of the fully supersonic started flow captured the thick floor boundary layer, the thin ceiling boundary in the isolator, the three compression ramp shock reflections, the inlet shoulder expansion fan, and subsequent expansion reflections. The data appeared to be consistent with shock-expansion theory and with previous schlieren imaging. Furthermore, the PIV data were able to successfully resolve the flow structure during unstart, which represented a much more challenging task. The flow structure, as seen by the PIV, was consistent with the schlieren imaging.

The PIV measurements show that shock-induced separation plays a critical role in the unstart process. As the unstart shock system propagates upstream the strength of separation increases and reverse flow velocities up to about $0.4U_\infty$ are induced both near the ceiling and the floor. The location of flow separation during unstart is

dependent on the locations where the reflected inlet shock impinges on the isolator walls. In particular, the flow separation intensifies as the unstart shock system reaches locations near the ceiling and floor impingement points of the initial inlet shock reflections. Since these impingement points are regions with preexisting adverse pressure gradients and hence locally thicker boundary layers, it appears that the unstart shock system progresses upstream taking the "path of least of resistance." These observations suggest that the inlet geometry may play a critical role in unstart dynamics because it will depend on the locations where the inlet shocks impinge on the walls of the isolator. The plan-view PIV measurements show that unstart progresses through the isolator first with separation of the sidewall boundary layers. Therefore, unstart in the low-aspect-ratio model was a highly three-dimensional event. The importance of boundary layer separation to the unstart process suggests that passive or active control devices that energize the isolator boundary layers may be effective at controlling or influencing the unstart process.

References

[1] Curran, E. T., and Stull, F. D., "The Utilization of Supersonic Combustion Ramjet Systems at Low Mach Numbers," Aero Propulsion Lab., Rept. RTD-TDR-63-4097, Wright–Patterson Air Force Base, OH, Jan. 1964.

[2] Curran, E. T., Heiser, W. H., and Pratt, D. T., "Fluid Phenomena in Scramjet Combustion Systems," *Annual Review of Fluid Mechanics*, Vol. 28, Jan. 1996, pp. 323–360.
doi:10.1146/annurev.fl.28.010196.001543

[3] Heiser, W. H., and Pratt, D. T., *Hypersonic Air Breathing Propulsion*, AIAA Education Series, AIAA, New York, 1993.

[4] Emami, S., Trexler, C. A., Auslender, A. H., and Weidner, J. P., "Experimental Investigation of Inlet-Combustor Isolators for a Dual Mode Scramjet at a Mach Number of 4," NASA TP-3502, May 1995.

[5] Wang, C.-P., Zhang, K.-Y., and Cheng, K.-M., "Pressure Distribution Measurements in Scramjet Isolators Under Asymmetric Supersonic Flow," AIAA Paper 2006-818, Jan. 2006.

[6] Bachchan, N., and Hillier, R., "Effects of Hypersonic Inlet Flow Non-Uniformities on Stabilising Isolator Shock Systems," AIAA Paper 2004-4716, Aug. 2004.

[7] Matsuo, K., Miyazato, Y., and Kim, H.-D., "Shock Train and Pseudoshock Phenomena in Internal Gas Flows," *Progress in Aerospace Sciences*, Vol. 35, No. 1, 1999, pp. 33–100.
doi:10.1016/S0376-0421(98)00011-6

[8] Waltrup, P. J., and Billig, F. S., "Structure of Shock Waves in Cylindrical Ducts," *AIAA Journal*, Vol. 11, No. 10, 1973, pp. 1404–1408.
doi:10.2514/3.50600

[9] Waltrup, P. J., and Billig, F. S., "Prediction of Precombustion Wall Pressure Distributions in Scramjet Engines," *Journal of Spacecraft and Rockets*, Vol. 10, No. 9, 1973, pp. 620–622.
doi:10.2514/3.27782

[10] Reinartz, B. U., Herrmann, C. D., and Ballmann, J. B., "Aerodynamic Performance Analysis of a Hypersonic Inlet Isolator Using Computation and Experiment," *Journal of Propulsion and Power*, Vol. 19, No. 5, 2003, pp. 868–875.
doi:10.2514/2.6177

[11] Sullins, G., and McLafferty, G., "Experimental Results of Shock Trains in Rectangular Ducts," AIAA Paper 92-5104, Dec. 1992.

[12] Tam, C.-J., Lin, K-C., Davis, D. L., and Behdadnia, R., "Numerical Investigations on Simple Variable Geometry for Improving Scramjet Isolator Performance," AIAA Paper 2006-4509, July 2006.

[13] Stouffer, S. K., and Hagenmaier, M. A., "The Effect of Aspect Ratio on Isolator Performance," AIAA Paper 2001-0519, Jan. 2001.

[14] Anderson, G. Y., McClinton, C. R., and Weidner, J. P., "Scramjet Performance," *Scramjet Propulsion*, edited by E. T. Curran, and S. N. B. Murthy, Vol. 189, Progress in Astronautics and Aeronautics, AIAA, Reston, VA, 2000.

[15] Hudgens, J. A., and Trexler, C. A., "Operating Characteristics at Mach 4 of an Inlet Having Forward-Swept Sidewall-Compression Surfaces," AIAA Paper 92-3101, July 1991.

[16] Masuya, G., Komuro, T., Murakami, A., Shinozaki, N., Nakamura, A.,

and Murayama, O., "Ignition and Combustion Performance of Scramjet Combustors with Fuel Injection Struts," *Journal of Propulsion and Power*, Vol. 11, No. 2, 1995, pp. 301–307.
doi:10.2514/3.51425

[17] Van Wie, D. M., Kwok, F. T., and Walsh, R. F., "Starting Characteristics of Supersonic Inlets," AIAA Paper 96-2914, July 1996.

[18] Weiting, A. R., "Exploratory Study of Transient Unstart Phenomena in a Three-Dimensional Fixed-Geometry Scramjet Engine," NASA TN D-8156, March 1976.

[19] Rodi, P. E., Emami, S., and Trexler, C. A., "Unsteady Pressure Behavior in a Ramjet/Scramjet Inlet," *Journal of Propulsion and Power*, Vol. 12, No. 3, 1996, pp. 486–493.
doi:10.2514/3.24061

[20] Hawkins, W. R., and Marquart, E. J., "Two-Dimensional Generic Inlet Unstart Detection at Mach 2.5–5.0," AIAA Paper 95-6016, April 1995.

[21] Shimura, T., Mitani, T., Sakuranaka, N., and Izumikawa, M., "Load Oscillations Caused by Unstart of Hypersonic Wind Tunnels and Engines," *Journal of Propulsion and Power*, Vol. 14, No. 3, 1998, pp. 348–353.
doi:10.2514/2.5287

[22] O'Byrne, S., Doolan, M., Olsen, S. R., and Houwing, A. F. P., "Analysis of Transient Thermal Choking Processes in a Model Scramjet Engine," *Journal of Propulsion and Power*, Vol. 16, No. 5, 2000, pp. 808–814.
doi:10.2514/2.5645

[23] Sato, T., and Kaji, S., "Study on Steady and Unsteady Unstart Phenomena due to Compound Choking and/or Fluctuations in Combustor of Scramjet Engines," AIAA Paper 92-5102, Dec. 1992.

[24] Neaves, M. D., McRae, S., and Edwards, J. R., "High-Speed Inlet Unstart Calculations Using an Implicit Solution Adaptive Mesh Algorithm," AIAA Paper 2001-0825, Jan. 2001.

[25] McDaniel, K. S., and Edwards, J. R., "Simulation of Thermal Choking in a Model Scramjet Combustor," AIAA Paper 99-3411, June 1999.

[26] McDaniel, K. S., and Edwards, J. R., "Three-Dimensional Simulation of Thermal Choking in a Model Scramjet Combustor," AIAA Paper 2001-0382, Jan. 2001.

[27] Wagner, J. L., Valdivia, A., Yuceil, K. B., Clemens, N. T., and Dolling, D. S., "Experimental Investigation of Unstart in an Inlet/Isolator Model in Mach 5 Flow," *AIAA Journal*, Vol. 47, No. 6, 2009, pp. 1528–1542.
doi:10.2514/1.40966

[28] Wagner, J. L., "Experimental Studies of Unstart Dynamics in Inlet/Isolator Configurations in a Mach 5 Flow," Ph.D. Dissertation, Department of Aerospace Engineering and Engineering Mechanics, Univ. of Texas at Austin, TX, 2009.

[29] Unalmis, O. H., and Dolling, D. S., "Decay of Wall Pressure Field and Structure of a Mach 5 Adiabatic Turbulent Boundary Layer," AIAA Paper 94-2363, June 1994.

[30] Unalmis, O. H., and Dolling, D. S., "Decay of Fluctuating Wall-Pressure Field of a Mach 5 Turbulent Boundary Layer," *AIAA Journal*, Vol. 37, No. 9, 1999, pp. 1088–1096.

doi:10.2514/2.837

[31] White, F. M., *Viscous Fluid Flow*, McGraw–Hill, Boston, 1991.

[32] Barter, J. W., "Prediction and Passive Control of Fluctuating Pressure Loads Produced by Shock-Induced Turbulent Boundary Layer Separation," Ph.D. Dissertation, Department of Aerospace Engineering and Engineering Mechanics, Univ. of Texas at Austin, TX, 1995.

[33] Hou, Y. X., "Particle Image Velocimetry Study of Shock Induced Turbulent Boundary Layer Separation," Ph.D. Dissertation, Department of Aerospace Engineering and Engineering Mechanics, Univ. of Texas at Austin, TX, 2003.

[34] Keane, R. D., and Adrian, R. J., "Theory of Cross-Correlation Analysis of PIV Images," *Applied Scientific Research*, Vol. 49, No. 3, 1992, pp. 191–215.
doi:10.1007/BF00384623

[35] Melling, A., "Tracer Particles and Seeding for Particle Image Velocimetry," *Measurement Science and Technology*, Vol. 8, No. 12, 1997, pp. 1406–1416.
doi:10.1088/0957-0233/8/12/005

[36] Erbland, P. J., "Development and Application of Carbon Dioxide Enhanced Rayleigh Scattering for High Speed Low Density Flows," Ph.D. Thesis, Princeton Univ., Princeton, NJ, 2000.

[37] Samimy, M., and Lele, S. K., "Motion of Particles with Inertia in a Compressible Free Shear Layer," *Physics of Fluids. A, Fluid Dynamics*, Vol. 3, No. 8, 1991, pp. 1915–1923.
doi:10.1063/1.857921

[38] Beresh, S. J., "The Effect of the Incoming Turbulent Boundary Layer on a Shock-Induced Separation Flow Using Particle Image Velocimetry," Ph.D. Dissertation, Department of Aerospace Engineering and Engineering Mechanics, Univ. of Texas at Austin, TX, 1999.

[39] Beresh, S. J., "The Influence of Velocity Gradients on PIV Measurements of Turbulence Statistics: A Preliminary Study," AIAA Paper 2008-3710, June 2008.

[40] Scarano, F., and Riethmuller, M. L., "Advances in Iterative Multigrid PIV Image Processing," *Experiments in Fluids*, Vol. 29, No. 7, 2000, pp. S51–60.
doi:10.1007/s003480070007

[41] Westerweel, J., "Fundamentals of Digital Particle Image Velocimetry," *Measurement Science and Technology*, Vol. 8, No. 12, 1997, pp. 1379–1392.
doi:10.1088/0957-0233/8/12/002

[42] Ganapathisubramani, B., Clemens, N. T., and Dolling, D. S., "Effects of Upstream Boundary Layer on the Unsteadiness of Shock-Induced Separation," *Journal of Fluid Mechanics*, Vol. 585, Aug. 2007, pp. 369–394.
doi:10.1017/S0022112007006799

E. Gutmark
Associate Editor